actuators

MDPI

Article

Sensorless Control of Linear Motion in a Linear-Rotary Reluctance Actuator Integrated into an Electromagnetic Dog Clutch

Bogdan Miroschnitschenko

Faculty of Engineering & Natural Sciences, Johannes Kepler University, 4040 Linz, Austria; miroshbogdan@gmail.com or bogdan.miroschnitschenko@jku.at

Abstract

A reluctance actuator integrated into the double-sided dog clutch of a gearbox can significantly simplify the gear shifting system. However, its disadvantage is that an axial position sensor is required to shift the neutral gear. The sensor is placed in the aggressive environment of a gearbox and reduces the reliability of the entire system. Sensorless methods proposed in the literature deal with electrical machines or actuators with one degree of freedom (linear motion or rotation). In the dog clutch, the shift sleeve rotates and moves along its rotation axis simultaneously, moreover, the coil inductances are highly dependent not only on the axial position but also on the relative angular position between the shift sleeve teeth and the slots of its counterpart. This work proposes an original algorithm of sensorless control, which main novelty is the applicability for systems with two degrees of freedom, such as the considered actuator. The voltage induced in one of the coils and the prediction of the shift sleeve motion, which is based on the electromechanical model of the clutch, are used to control the currents. Not only an axial position sensor but also angular encoders are not required to apply the proposed method. The algorithm was tested both in simulations and experiments under different conditions. The results show that the proposed method allows to shift the neutral gear sensorless at different rotation speeds and different loads on the sleeve, regardless of what gearwheel is initially engaged.

Keywords: sensorless; control; linear-rotary actuator; gear shifting; dog clutch; gearbox

check for updates

Academic Editor: Xiaoping Liu

Received: 21 August 2025
Revised: 22 September 2025
Accepted: 30 September 2025
Published: 4 October 2025

Citation: Miroschnitschenko, B. Sensorless Control of Linear Motion in a Linear-Rotary Reluctance Actuator Integrated into an Electromagnetic Dog Clutch. *Actuators* **2025**, *14*, 484. https://doi.org/10.3390/act14100484

Copyright: © 2025 by the author. Licensee MDPI, Basel, Switzerland. This article is an open access article distributed under the terms and conditions of the Creative Commons Attribution (CC BY) license (https://creativecommons.org/licenses/by/4.0/).

1. Introduction

Reluctance actuators integrated into a dog clutch [1,2] represent a promising solution for the simplification of actuating systems used for gear shifting in automotive area. Installed inside the gearbox directly between two gearwheels, the actuator shifts the required gear by exciting one of two coils. The arisen reluctance force moves the shift sleeve in the corresponding direction engaging its teeth with the slots of the complementary part placed on the gearwheel. This solution demonstrates much lower complexity comparing with common systems, where the shift sleeve is actuated with a fork connected to a rotary motor outside the gearbox via several intermediate parts required to transform the rotary motion of the motor to the linear motion of the fork [3–8].

Moreover, the function of the shifting actuator is not restricted only with the linear displacement of the shift sleeve. In my previous publication [9], I showed that a contactless synchronization of the gearwheel and shift sleeve speeds becomes possible simply by adding teeth on the counterpart of the shift sleeve. So, in the addition to the axial force,

a reluctance torque can be generated like in a homopolar switched reluctance machine (SRM) [10], and the linear reluctance actuator becomes a linear-rotary reluctance actuator (LRRA), which can be designed and optimized using the method developed in [11]. This solution demonstrates how not only an external actuation system but also synchromesh units, which operation principle is based on the friction between the rotating parts and inevitably creates wear problems [12,13], can be simultaneously replaced by the integrated shifting device. A novel double-sided electromagnetic dog clutch [14] has been further developed on the basis of one-sided clutch [9], both topologies are included in the pending patent application [15]. In the neutral gear, the speed difference between the shift sleeve and one of the gearwheels can be reduced contactless using the torque generated by the clutch [14]. The information about the relative angular positions and speeds on both sides is required for torque generation; moreover, it can be also used to chose an optimal time for gear shifting [1]. The relative angle and speed difference can be estimated on each side of the developed LRRA without angular encoders using the method proposed later in [16].

Three different gears can be selected with the double-sided clutch, i.e., the left, right and neutral gears (Figure 1). The left and right gears can be shifted by engaging the sleeve teeth with the slots of the complementary ring mounted on the corresponding gearwheel. In this case, the information about the axial position x of the shift sleeve is not required since the sleeve stops automatically at the required end-position by a mechanical contact between the face surfaces of the teeth and bottoms of the slots. However, shifting into neutral is much more complex since the neutral gear position ($x = 0$) is in the middle between the motion limits (-8 mm and 8 mm). The coil currents on both sides must be actively controlled based on the actual axial position of the sleeve to stop it at $x = 0$. So, a linear encoder (sensor) is required. It can be placed on one of the stators or on the hub to measure x. In any case, the sensor is exposed to the aggressive environment of transmission oil mixed with metal particles arisen due to the wear of the parts, which creates a high failure probability. Thus, the development of a sensorless control algorithm becomes a much more attractive alternative.

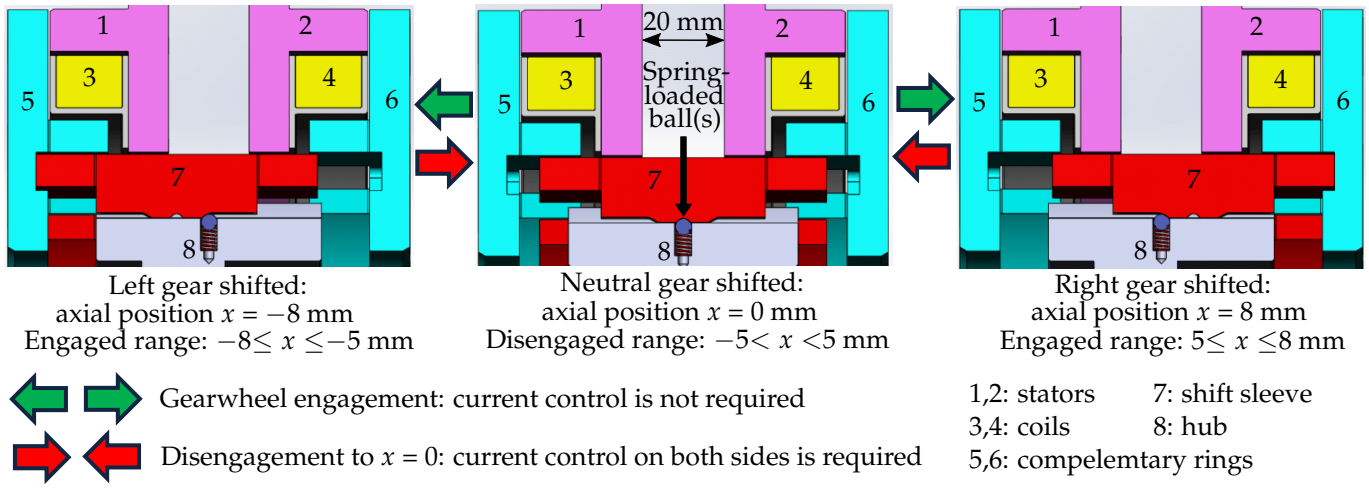

Figure 1. Clutch states depending on the axial position of the shift sleeve.

Various techniques of sensorless control have been proposed for linear actuators in the scientific literature. Sensorless estimation of the plunger position based on the incremental inductance [17,18] or resonance frequency [19] has been developed for solenoid valve actuators. Sliding mode control has been applied in an electromagnetic valve actuator with two coils [20], in a solenoid electromagnet (SE) for fuel injection [21], and in a fast-switching SE [22]. Sensorless position estimation and control using direct inductance measurement has been developed for a SE in [23]; later, the authors of this work have

proposed the evaluation of eddy current losses in [24] to solve the problem of ambiguities in position estimation caused by a non-monotonic dependency of the incremental inductance over the position in SEs. A method that uses an injection of an additional AC signal has been developed for sensorless position estimation [25] and control [26] in a compact dual solenoid actuator. In a reluctance actuator with two coils and a permanent magnet on the stator, the mover position has been estimated using the back electromotive force [27]. Methods of sensorless control based on the change of the eddy current losses [28] or the current waveform [29] have been also developed for SEs. Moreover, some authors have proposed designs of linear actuators with emphasis of self-sensing properties [30,31].

Despite the methods of sensorless control in linear actuators have been well studied, none of the techniques described in [17–31] are suitable for the LRRA considered in this paper for different reasons. Firstly, the size of its magnetic circuit is several times bigger compared to that of the SEs presented in [17,19,21,22,25,26,29], so the influence of eddy current effects is much stronger. High eddy currents in the solid magnetic circuit significantly reduce the capabilities of sensorless control, so some papers even propose the use of laminated steel [30]. Secondly, the shift sleeve moves with much higher velocities than the plungers of the SEs for which the methods from [17,18,23–26,28,30] have been applied. Thirdly, high deviations between the estimated and real positions [27] are not crucial in the actuators where the required end-positions correspond to mechanical limits of the motion, but are unacceptable in the proposed clutch, where the neutral gear position is in the middle between the motion limits. But the main problem is that all these publications consider actuators with one degree of freedom (DoF), which is translational motion, while the shift sleeve of the LRRA has two DoFs since it moves axially and rotates simultaneously. Moreover, the inductances of both coils are highly dependent on the relative angular position between the teeth of the shift sleeve and slots of the complementary ring on the corresponding actuator side.

The possibilities of end-position detection in an actuator integrated into a one-sided dog clutch have been recently studied at the JKU Hoerbiger Research Institute for Smart Actuators [32]. However, the proposed method is not applicable for an active control of the shift sleeve movement due to a high error between the actual and estimated positions, it allows only to estimate reaching of the required end-position with a significant delay. Moreover, the dependency of the coil inductance on the relative angular position between the parts is not considered in [32]. To my best knowledge, no sensorless methods to control the linear motion in linear-rotary actuators have been proposed earlier in the literature.

Considering all the facts mentioned above, I develop in this paper a control algorithm for double-sided electromagnetic dog clutches, which makes shifting the neutral gear feasible without linear encoders. The electromechanical model of the device is described in the next section. It is applied in Section 3 to develop the method of sensorless disengagement to the neutral gear position. The algorithm is tested in simulations of different disengagement conditions in Section 4 and verified experimentally in Section 5. The results are concluded in Section 6.

2. Electromechanical Model

The operation principle and construction of the clutch (Figure 1), which is represented by the LRRA integrated between two gearwheels of a gearbox, is described in detail in [14]. The actuator contains the stators 1, 2 with the mounted in them coils 3, 4 and the left and right complementary rings 5, 6 rigidly connected to the left and right gearwheels [14], respectively. The parts are placed symmetrically on the left and right clutch sides. The sides are separated by an air gap of 20 mm, so the magnetic coupling between the coils is negligible. If the neutral gear is selected, the shift sleeve 7 is at the central axial position

$x = 0$. If one of the gears (left or right) has to be shifted, the sleeve can be moved axially on the hub 8, which is installed on the output shaft of the gearbox, by exciting the coil on the corresponding side. The arisen reluctance force engages the teeth with the slots of the complementary ring coupling the shaft with the gearwheel mechanically. The left and right gears have different gear ratios (44/64 and 64/44, respectively), so if the countershaft of the gearbox rotates, different relative angular speeds $n_{rel\,left}$, $n_{rel\,right}$ and positions $\theta_{rel\,left}$, $\theta_{rel\,right}$ between the sleeve teeth and the slots of the complementary rings are presented on the sides. The teeth of the complementary rings are placed above the slots and allow a preliminary electromagnetic synchronization of the rotation speeds [14] and also sensorless estimation of the relative angular speed and positions between the shaft and the gearwheels [16], but do not take part in the mechanical coupling. There are nine tooth pairs on each side, so $\theta_{rel\,left}$ and $\theta_{rel\,right}$ change periodically between $-20°$ and $20°$.

When the sleeve reaches the positions $x = -8$ mm (left gear shifting) or $x = 8$ mm (right gear shifting), its further axial movement is prevented by the mechanical contact between the sleeve and the ring, so that an active current control is not necessary to shift the left or right gear. When switching back to the neutral gear is required, the coil on the disengaged side is excited to release the teeth from the slots. Soon after the motion starts, this coil has to be de-excited again, and the coil on the previously engaged side is excited a little later to brake the motion and stop the sleeve around the axial position $x = 0$. After that, the braking coil has to be de-excited rapidly. Thus, an active control of both coil currents is required to shift the neutral gear.

Three spring-loaded balls placed in the notches of the hub generate the axial force F_{spring} if the sleeve is located axially close to the positions $x = \pm 8$ mm and $x = 0$ mm (Figure 2). There, negative values of F_{spring} mean that the force is directed to the left, and the positive sign means that it is directed to the right. This is also true for all further forces described in this paper. Thus, F_{spring} prevents self-disengagement of the clutch if the left or right gear is shifted, or self-displacement of the shift sleeve from the central axial position $x = 0$ if the neutral gear is selected. Moreover, when the sleeve is being disengaged to the neutral gear position, the final centering at $x = 0$ is achieved under the influence of the spring-loaded balls.

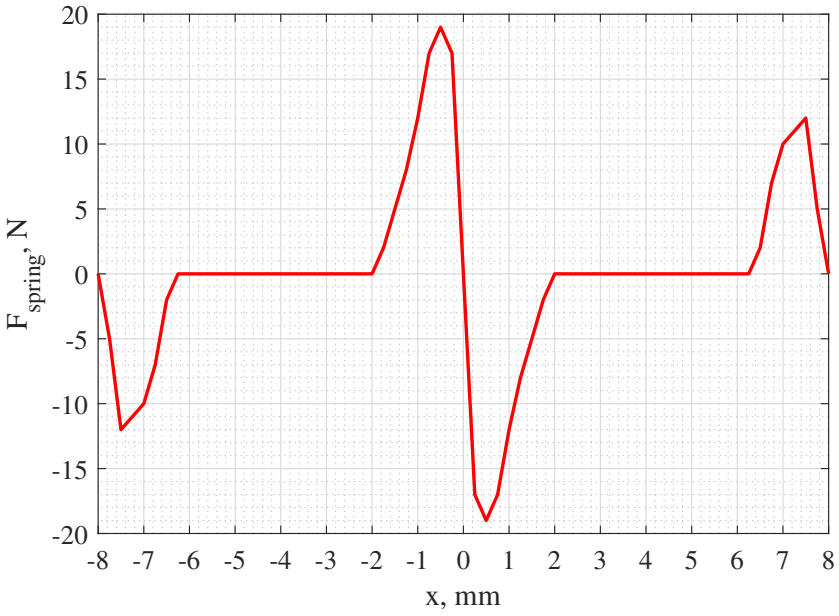

Figure 2. Axial force generated by the spring-loaded balls depending on the axial position of the shift sleeve.

In the neutral gear, the torque transmitted through the shift sleeve is zero. If the left or right gear is shifted, the clutch couples the driving motor with the output shaft mechanically by the angular contact between the sleeve teeth and the slots of the corresponding complementary ring. The resulting torque which acts on the shift sleeve T_{sleeve} is the difference between the torque $T_{gear\,eng}$ on the engaged gearwheel and the torque T_{shaft} on the output shaft:

$$T_{sleeve} = T_{gear\,eng} - T_{shaft}. \tag{1}$$

$T_{gear\,eng}$ can be estimated from the torque of the driving motor T_{motor}, the friction torque on the countershaft $T_{c\,fr}$, the gear ratio on the engaged side g_{eng} and the total electromagnetic torque on the engaged side $T_{act\,eng}$, which is generated by the actuator:

$$T_{gear} = (T_{motor} - T_{c\,fr})g_{eng} + T_{act\,eng}. \tag{2}$$

$T_{act\,eng}$ is calculated based on the gear ratios and the electromagnetic torques $T_{elmag\,eng}$ and $T_{elmag\,diseng}$ that arise between the teeth of the sleeve and complementary ring on the engaged and disengaged side, respectively, when the corresponding coil is excited [14]:

$$T_{act\,eng} = T_{elmag\,diseng}\frac{g_{eng}}{g_{diseng}} + T_{elmag\,eng}, \tag{3}$$

where g_{diseng} is the gear ratio on the disengaged side. The actuator generates torques with the same principle as a SRM [14]. A nearly full radial alignment is presented between the teeth of the sleeve and complementary ring on the engaged side, so $T_{elmag\,eng} \approx 0$.

Since the angular backlash exists due to the difference in the angular lengths of the slots τ_s and teeth τ_t, and there is some clearance between the hub and the sleeve defined by the tolerances of their splines (Figure 3a), a non-zero T_{sleeve} tilts the shift sleeve and generates the tilting force F_{tilt} (Figure 3b), which can be calculated using the following equation:

$$F_{tilt} = \pm\frac{T_{sleeve}}{r}\tan\beta, \tag{4}$$

where r is the sleeve radius (r = 61.5 mm in the manufactured prototype) and β is the tilting angle, which maximum value is defined by the spline tolerances and is relative small (less than 0.5° in the considered clutch). This force tends to push the teeth out of the slots, so, its sign is negative if the right gear is engaged. F_{tilt} can lead to the self-disengagement of the clutch. At lower values of T_{sleeve}, the force F_{spring} generated by the spring-loaded balls is much higher than the tilting force and keeps the sleeve engaged. However, F_{spring} can become lower than F_{tilt} at higher values of T_{sleeve}. Therefore, a DC-voltage of a constant value is applied to the coil on the engaged side to excite it with the current I_{eng}, so that the flux linkage on the engaged side Ψ_{eng} arises and generates the holding force F_{hold}, which keeps the shift sleeve at the position of full engagement. Since the distance between the surfaces of the teeth and slots is close to zero, significant values of Ψ_{eng} and F_{hold} can be achieved at low current values, so that the power losses are negligible, and there is no danger of coil overheating. Figure 4 shows the values of flux linkage and holding force on the engaged side obtained using 3D finite element analysis (3D FEA) in Ansys Electronics.

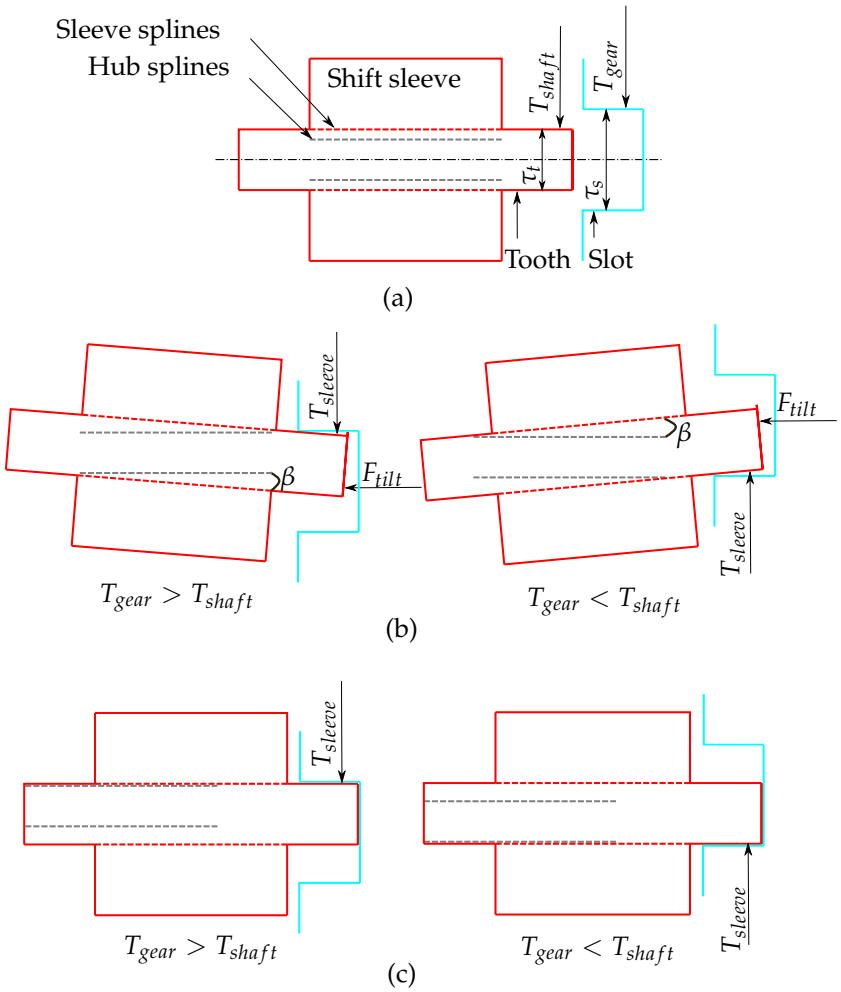

Figure 3. Torque and tilting force on the shift sleeve depending on the sleeve state: (**a**) disengaged; (**b**) partially engaged; (**c**) full engagement. The red part is the shift sleeve, the blue part is the complementary ring.

When the gear has to be switched, the motor torque can be controlled to reduce T_{sleeve} and, consequently, the friction between the side surfaces of the sleeve teeth and ring slots. The friction force F_{fr} is calculated as

$$F_{fr} = -sign(v)\left(mg + \frac{|T_{sleeve}|}{r}\right)\mu, \tag{5}$$

where v is the axial speed (the friction is always opposite to the motion direction), m is the shift sleeve mass (∼1.75 kg), g = 9.81 m/s^2, and μ is the friction coefficient, which can be assumed equal to 0.03 [33] for the supposed application environment of the clutch (gearbox filled with transmission oil). The term mg in (5) represents the contact force between the sleeve and the hub, and the term $|T_{sleeve}|/r$, which is the contact force between the sleeve and the ring, becomes zero if the teeth are disengaged. Exciting the coil on the disengaged side with the current I_{diseng} generates the electromagnetic force F_{diseng}, and the axial motion starts if $|F_{diseng}| > |F_{srping} + F_{fr} + F_{hold}|$. The additional teeth on the complementary rings not only allow the pre-synchronization of the rotation speeds in the neutral gear [14] but also significantly increase the disengaging coil inductance L_{diseng} and the disengaging force as following. Figure 5 shows the characteristics of L_{diseng} and F_{diseng} depending on the axial position x and the absolute value of the relative angular position on the disengaging side $|\theta_{rel\ diseng}|$, where $|\theta_{rel\ diseng}| = 0°$ corresponds to the full radial overlapping between the

sleeve teeth and ring teeth. It can be seen that the disengaging force rises significantly with the increase of the teeth overlapping.

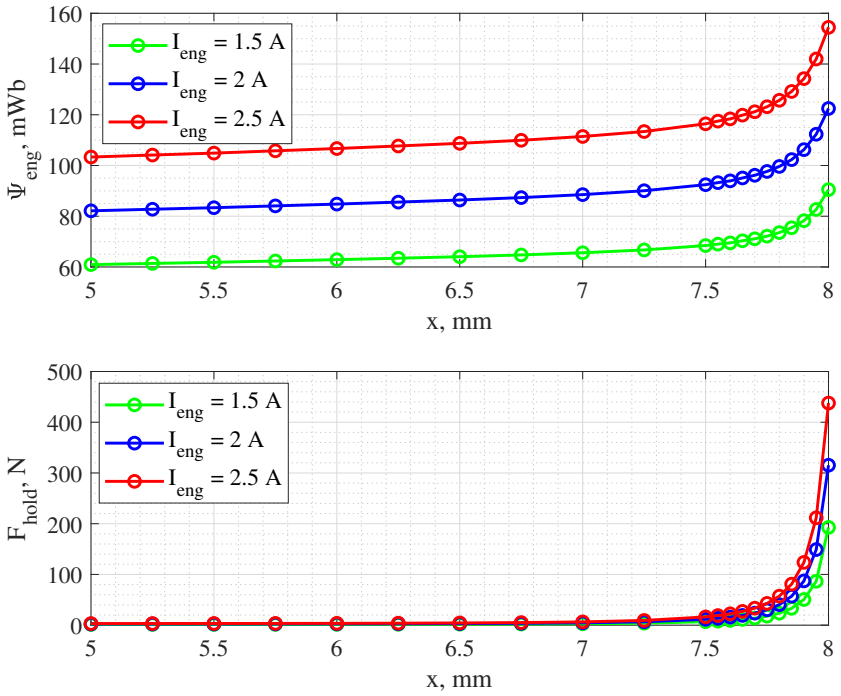

Figure 4. Flux linkage and holding force on the engaged side depending on the coil current and axial position of the sleeve (results of 3D FEA), characteristics for the right gearwheel disengagement. For the left gearwheel disengagement, x and F_{hold} are multiplied by -1.

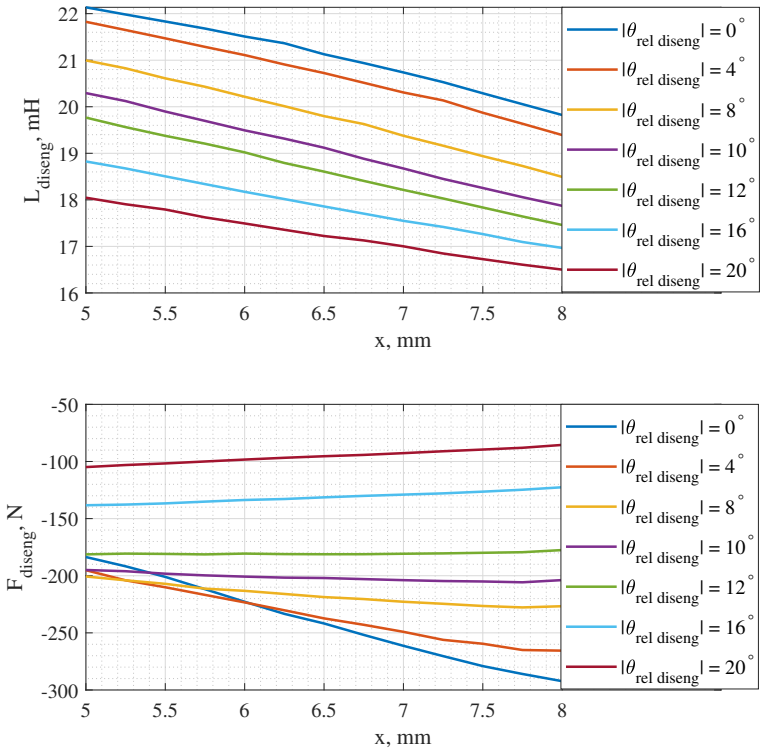

Figure 5. Coil inductance and force on the disengaging side depending on the relative angular position and axial position of the shift sleeve at I_{diseng} = 19 A (results of 3D FEA). Characteristics for the right gearwheel disengagement. For the left gearwheel disengagement, x and F_{diseng} are multiplied by -1.

The holding force F_{hold} can be easily made equal to zero by de-exciting the coil on the engaged side. However, if it remains excited, the axial motion of the sleeve during the disengagement causes the change of the flux linkage Ψ_{eng} and induces the voltage U_{ind} in the coil. The holding force on the engaged side becomes negligible soon after the teeth start to leave the slots ($F_{hold} \approx 0$ if $|x| < 7.5$ mm, Figure 4). The induced voltage is calculated as

$$U_{ind} = -\frac{d\Psi_{eng}}{dt} \tag{6}$$

and can be used to estimate the axial position of the shift sleeve without an axial position sensor. The method of sensorless control based on the measurement of U_{ind} is described in the next section.

Since F_{hold} disappears quickly when the motion starts, the axial speed of the sleeve v keeps increasing if the current I_{diseng} on the disengaged side is applied and generates F_{diseng}. De-exciting the disengaging coil stops the acceleration. When the sleeve moves in the ranges of x where the axial force generated by the spring-loaded balls F_{spring} is non-zero ($|x| > 6.25$ mm or $|x| < 2$ mm, Figure 2), the damping force F_d arises. This force reduces the kinetic energy of the sleeve and is linearly proportional to the speed v:

$$F_d = -cv, \tag{7}$$

where c is the damping coefficient, which is the function of the sleeve mass m, the stiffness factor of the springs k, the number of spring-loaded balls N_b, and the damping ratio ζ:

$$c = 2\zeta\sqrt{N_b k m}. \tag{8}$$

Three spring-loaded balls are placed in the hub ($N_b = 3$), and k of the used springs is 2767 N/m. Assuming that $\zeta = 0.4$ (under-damped system), c can be estimated equal to 96 Ns/m.

As soon as the shift sleeve reaches the position $|x| = 6.25$ mm during the disengagement, F_d becomes zero, and its kinetic energy is only reduced by the friction force F_{fr}, which almost disappears when the teeth leave the slots ($|x| < 5$ mm, Equation (5)). Thus, the motion speed v of the sleeve remains approximately constant in the range of $|x|$ between 5 and 2 mm. The coil on the side which is being disengaged must be excited with a higher current value to generate the braking force F_{brake} and reduce the speed when the sleeve approaches the central position $x = 0$. If v is relatively low and $|x| < 2$ mm, the residual motion is slowed down under the influence of the forces F_{spring} and F_d generated by the spring-loaded balls, and the sleeve is centered at the neutral gear position $x = 0$ by F_{spring}.

The characteristics of the inductance L_{brake} and force F_{brake} on the braking side are shown in Figure 6 for different values of the braking current I_{brake}. On the side which is being disengaged, the relative angular speed does not become significantly greater than zero after the teeth leave the slots, so the relative angular position on the braking side $\theta_{rel\ brake}$ has been chosen equal to 0° for the calculation of the characteristics shown in Figure 6 using 3D FEA.

The total axial force F_{sleeve} which acts on the shift sleeve during the disengagement is the sum of the electromagnetic F_{elmag} and mechanical F_{mech} forces:

$$F_{sleeve} = F_{elmag} + F_{mech}. \tag{9}$$

$F_{elmag} = F_{diseng} + F_{hold}$ at the start of disengagement, and $F_{elmag} = F_{brake}$ when the motion is being braked. F_{mech} represents the sum of the mechanical force components, which are the tilting, spring, friction, and damping forces:

$$F_{mech} = F_{tilt} + F_{spring} + F_{fr} + F_d. \tag{10}$$

Assuming that the torque on the sleeve T_{sleeve} is in the range between $0 < |T_{sleeve}| < 25$ Nm when the gear is being switched, and the maximum value of $|v|$ is limited with 0.75 m/s, the variation ranges of the mechanical force components can be calculated using (4), (5), (7): $|F_{tilt}| = 0...3.5$ N, $|F_{fr}| = 0.5...12.7$ N, $|F_d| = 0...64$ N. The axial force of the spring-loaded balls F_{spring} is limited with the range $-19 \leq F_{spring} \leq 19$ N. So, F_{tilt}, F_{fr}, and F_{srping} are negligible compared to the electromagnetic force components, and (9) can be simplified to

$$F_{sleeve} \approx F_{elmag} + F_d. \tag{11}$$

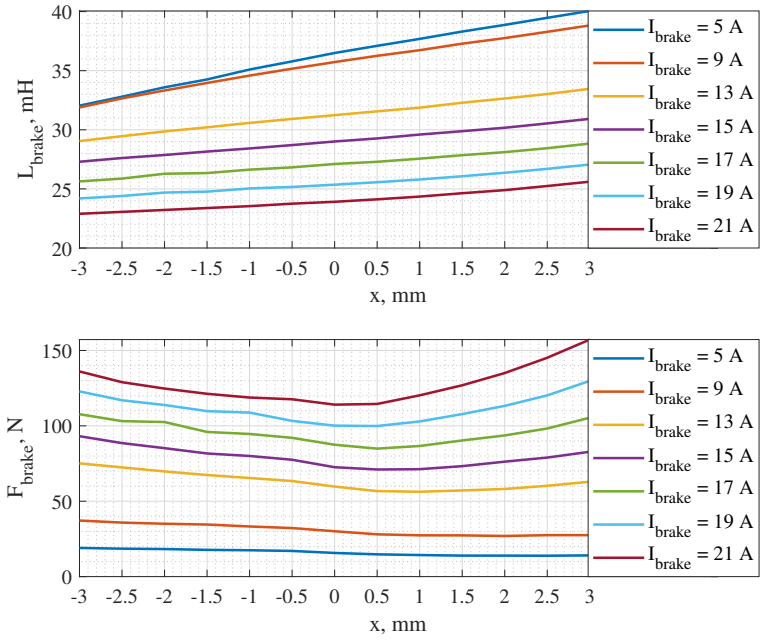

Figure 6. Coil inductance and force on the braking side depending on the axial position of the shift sleeve and braking current at $\theta_{rel\ brake} = 0°$ (results of 3D FEA). Characteristics for the right gearwheel disengagement. For the left gearwheel disengagement, x and F_{brake} are multiplied by -1.

Since Figures 4 and 5 show the results obtained using 3D FEA, the value of $x = 8$ mm corresponds there to the distance between the teeth and the slots equal to zero, as if the sleeve and the engaged ring were one part. However, it is not possible in the real clutch due to the flatness tolerances, surface roughness, and further deviations between the modeled and the real geometry. Thus, it can be assumed that the maximum values of F_{hold} and Ψ_{eng} at the corresponding currents are not higher than their values shown in Figure 4 for $x = 7.95$ mm. However, the holding force is still significant in this case. So, the axial motion of the sleeve can not start until $|\theta_{rel\ diseng}|$ is lower than some value $|\theta_{rel\ start}|$, where $|F_{diseng}| = |F_{hold} + F_{mech}|$. The range of the angular positions on the disengaging side where the start of the axial movement is possible can be named as starting range. At high relative speeds on the disengaging side, the initial value of $\theta_{rel\ diseng}$ does not play a significant role since the relative angular position changes very quickly, and it can be assumed that the average value of the disengaging force $F_{diseng\ av}$ corresponds to the value of F_{diseng} at the average $|\theta_{rel\ diseng}|$, which is 10° (Figure 5). At low relative speeds, there can be some delay between the start of the disengagement and the begin of the axial motion

if the initial $|\theta_{rel\ diseng}|$ is not in the starting range. An average disengaging force $F_{diseng\ av}$ can be assumed from Figure 5 considering the range of $|\theta_{rel}|$ between 0° and $|\theta_{rel\ start}|$ if the rotation speed difference on the disengaging side is low.

After the axial motion of the shift sleeve is started, the holding force disappears quickly, and the average axial force $F_{sleeve\ av}$ applied to the sleeve can be assumed equal to $F_{diseng\ av} + F_d$ when $|x|$ becomes less than 7.5 mm. So, the sleeve acceleration a is approximately constant and has some average value $a_{av} = F_{diseng\ av}/m$ until the disengaging coil is de-excited. In the range of motion between the end of acceleration and start of braking, $F_{sleeve\ av}$ is approximately zero. When the braking position is reached, the braking coil is excited with a higher current and generates the braking force of some average value $F_{brake\ av}$, which can be estimated from Figure 6 for the desired braking current I_{brake} assuming the range of x where the motion is braked. In this case, $F_{sleeve\ av} \approx F_{brake\ av} + F_d$, and the sleeve moves with approximately constant deceleration until the braking coil is de-excited.

Based on the assumptions from the previous paragraph, the axial displacement of the shift sleeve during the disengagement to the neutral gear can be considered as a motion with constant ac-/deceleration. This allows to develop the method of motion control without axial position sensors in the next section.

3. Method of Sensorless Disengagement to the Neutral Gear Position

If the shift sleeve moves with a constant acceleration (deceleration) of the value a, its axial position x and axial speed v are described with the following equations:

$$v = v_0 + at = v_0 + \frac{F_{sleeve\ av}}{m}t, \tag{12}$$

$$x = x_0 + vt = x_0 + \frac{at^2}{2} = x_0 + \frac{F_{sleeve\ av}}{2m}t^2, \tag{13}$$

where t is the time elapsed after the start of motion, v_0 is the initial axial speed ($v_0 = 0$), and x_0 is the initial axial position ($x_0 = \pm 8$ mm, where the negative and positive sign correspond to the disengagement of the left and right gearwheel, respectively). Omitting the non-linearity of the holding force and the influence of the mechanical forces, it can be assumed that $F_{sleeve\ av}$ rises linearly when the motion begins, so that its values are 0 at the position x_0 and $F_{diseng\ av}$ at the position x_1, respectively, (x_1 is the position where the holding force almost disappears, $x_1 \approx \pm 7.5$ mm, as mentioned above). So, the speed v_1, which is reached by the shift sleeve at the position x_1, can be calculated as

$$v_1 \approx \sqrt{\frac{4m(x_1 - x_0)}{F_{diseng\ av}\varepsilon_f}}\frac{F_{diseng\ av}\varepsilon_f}{2m}, \tag{14}$$

where $F_{diseng\ av}$ is chosen based on the characteristic of F_{diseng} for $|\theta_{rel\ diseng}| = 10°$, and ε_f is the factor that considers the force reduction under the influence of eddy currents, $\varepsilon_f \approx 0.9$. Defining the speed v_2 at which the de-excitation of the disengaging coil has to be started, the time $t_{diseng\ off}$ required to accelerate the sleeve from v_1 to v_2 can be calculated as

$$t_{diseng\ off} = \frac{v_2 - v_1}{F_{diseng\ av}\varepsilon_f - \chi_1(v_2 + v_1)c}m, \tag{15}$$

where χ_1 is the factor that considers how long the spring-loaded balls act during the acceleration. If the acceleration ends within the range $|x| > 6.25$ mm, $\chi_1 = 0.5$. Otherwise,

$\chi_1 < 0.5$. The axial position x_2 at which the de-excitation of the disengaging coil starts is consequently estimated as

$$x_2 = x_1 + \frac{v_2 + v_1}{2} t_{diseng\,off}. \tag{16}$$

The position x_2 can be estimated indirectly from the voltage U_{ind} induced in the coil on the engaged side. To demonstrate the possibility of the axial position estimation from the induced voltage, simulations of the following conditions have been conducted: the DC-voltage of a value $U_{eng} = I_{eng\,in} R_{eng}$ is applied to the coil on the engaged side, where $I_{eng\,in}$ is the initial current in this coil ($I_{eng\,in}$ is chosen equal to 1.5, 2, and 2.5 A), and R_{eng} = 0.75 Ohm is the resistance of this coil; all mechanical and electromagnetic forces are set to zero; instead of them, a constant disengaging force of the absolute values $|F_{diseng}|$ = 150, 175, and 200 N is applied to the sleeve, so that it moves with the constant acceleration $a = F_{diseng}/m$. Since the external force acts on the sleeve instead of the sum of the internal actuator forces, this can be considered as a fictive disengagement. Figure 7 shows the simulation results for some combinations of $|F_{diseng}|$ and $I_{eng\,in}$. Plotting the absolute values of the axial position x over U_{ind} (Figure 8), it can be concluded that U_{ind} is essentially independent on the force applied to the shift sleeve but has a clear correlation with the axial position x and the initial current on the engaged side $I_{eng\,in}$. So, the value of x can be indirectly estimated from U_{ind} if a constant DC-voltage is applied to the coil on the engaged side while the shift sleeve is accelerated by the force generated on the opposite side. The de-excitation of the disengaging coil starts when the voltage induced in the coil on the engaged side reaches the value $U_{ind\,off}$, which is obtained from the characteristics in Figure 8 based on the corresponding initial current on the engaged side and $|x| = |x_2|$. The time $t_{demag\,diseng}$ required to de-excite the disengaging coil and reduce its current from I_{diseng} to a negligible value can be estimated from the equation

$$t_{demag\,diseng} = -ln\left(1 - \frac{I_{diseng} R_{diseng}}{U}\right) \frac{L_{diseng}}{R_{diseng}} \varepsilon_t, \tag{17}$$

where L_{diseng} is the average value of the coil inductance on the disengaging side, which can be assumed equal to 19 mH for the disengaging current of 19 A (Figure 5), R_{diseng} is the resistance of this coil (R_{diseng} = 0.75 Ohm), U is the de-exciting voltage applied to the coil, which is equal to the supply voltage of 70 V, and ε_t is the factor which defines the influence of eddy currents on the (de)magnetization time. Using the simplified model of eddy currents proposed in the previous publication [16], ε_t can be estimated: $\varepsilon_t \approx 0.5$. Assuming that 50% of the disengaging force still acts on the shift sleeve while the coil is being de-excited, the final value of the motion speed v_3, to which the sleeve is accelerated by F_{diseng}, can be estimated as

$$v_3 = v_2 + \frac{0.5 F_{diseng\,av} \varepsilon_f}{m} t_{demag\,diseng}, \tag{18}$$

and the axial position x_3 where the sleeve speed reaches the value v_3 is obtained as

$$x_3 = x_2 + \frac{v_2 + v_3}{2} t_{demag\,diseng}. \tag{19}$$

If the disengaging current I_{diseng} and the speed v_2 are chosen correctly, x_3 is close to the range $5 < |x| < 2$ mm or within this range, where F_{tilt}, F_{spring}, and F_d are zero, and the motion is only braked by the friction between the sleeve and the hub, which is negligible. So, it can be assumed that the sleeve moves with the speed v_3 after the disengaging side becomes demagnetized. Defining the position where the coil on the side

which is being disengaged has to be excited to brake the motion as x_4, the time of delay t_{delay} between the start of the disengaging side demagnetization and the start of the braking side magnetization can be calculated as

$$t_{delay} = \frac{x_4 - x_3}{v_3} + t_{demag\,diseng}. \quad (20)$$

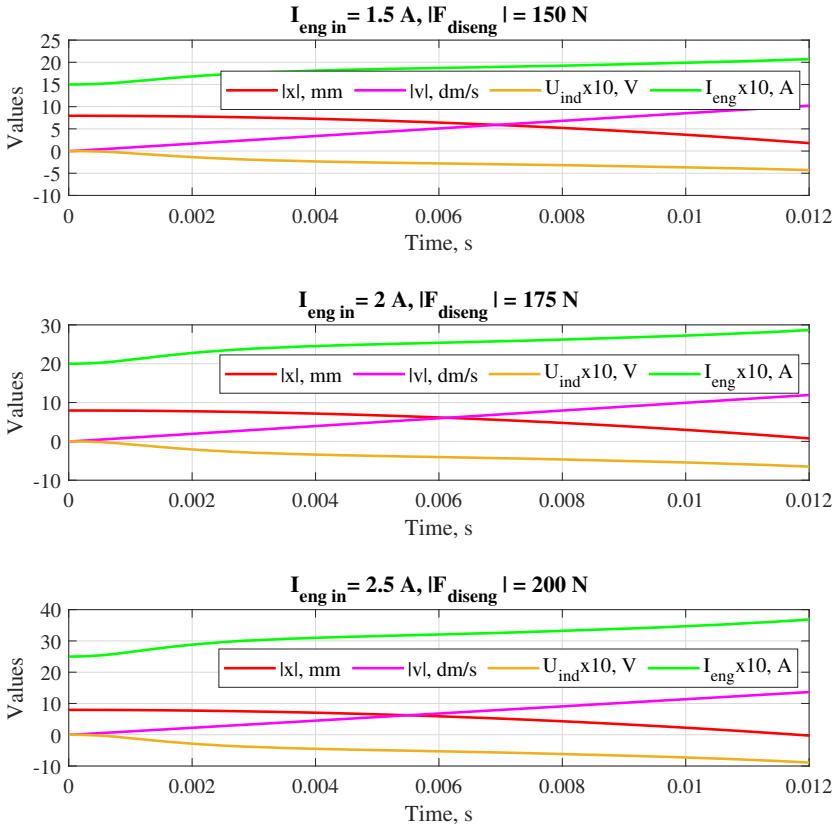

Figure 7. Simulation results of the fictive disengagement by applying different external forces to the sleeve at different values of the initial current on the engaged side.

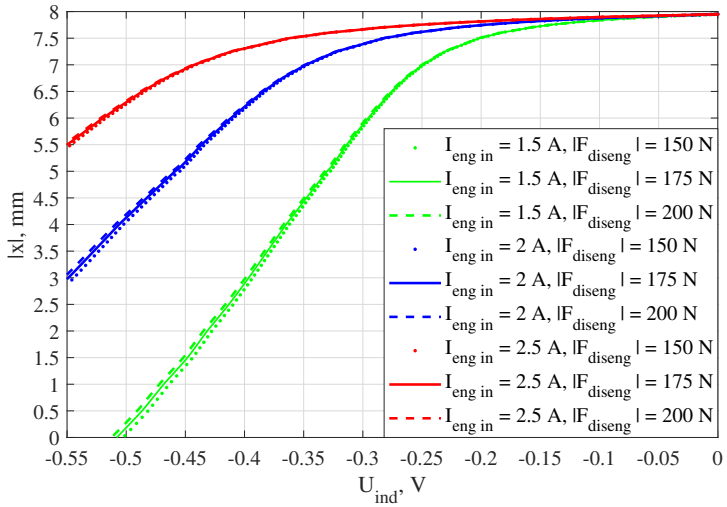

Figure 8. Voltage induced in the coil on the engaged side depending on the initial coil current and applied disengaging force.

The speed v_4 at the position x_4 can be estimated as

$$v_4 = v_3 \nu_1, \tag{21}$$

where ν_1 is the coefficient which considers the speed decrease caused by the damping force. If $|x_4| > 2$ mm, $\nu_1 = 1$, otherwise, $\nu_1 < 1$. The time $t_{mag\,brake}$ required to excite the braking coil can be calculated from

$$t_{mag\,brake} = -ln\left(1 - \frac{I_{brake} R_{eng}}{U}\right) \frac{L_{brake}}{R_{eng}} \varepsilon_t, \tag{22}$$

where L_{brake} is estimated using the inductance characteristic in Figure 6 based on the chosen braking current and the position where the excitation of the braking coil starts. Assuming that 50% of the braking force acts on the sleeve while the braking coil is being excited, the axial speed of the sleeve v_5 at which the braking coil excitation is finished and the corresponding axial position x_5 are calculated as

$$v_5 = v_4 + \frac{0.5 F_{brake\,av} \varepsilon_f - v_4 c \nu_2}{m} t_{mag\,brake}, \tag{23}$$

$$x_5 = x_4 + \frac{v_4 + v_5}{2} t_{mag\,brake}, \tag{24}$$

where ν_2 is the coefficient which considers the decrease of the speed during the time interval $t_{mag\,brake}$ caused by the damping force. If the braking coil is excited out of the range $|x| < 2$ mm, where the spring-loaded balls act, ν_2 becomes zero, meaning that no damping force acts on the sleeve. Otherwise, $\nu_2 < 1$.

Defining the desired speed at the end of braking as v_6, the time t_{brake} between the start of the braking coil excitation and the start of its de-excitation is calculated as

$$t_{brake} = t_{mag\,brake} + \frac{v_6 - v_5}{F_{brake\,av} \varepsilon_f - \chi_2 (v_5 + v_6) c} m, \tag{25}$$

where χ_2 is the factor that considers how long the spring-loaded balls act during the braking. If the braking ends within the range $|x| < 2$ mm, $\chi_2 = 0.5$. Otherwise, $\chi_2 < 0.5$. Finally, the axial position x_6 where the braking ends is calculated as

$$x_6 = x_5 + \frac{v_5 + v_6}{2} (t_{brake} - t_{mag\,brake}). \tag{26}$$

If x_6 is out of the range $|x_6| < 2$ mm, v_6 must be non-zero and directed to the center, so that the sleeve returns to the central position by the residual motion. Otherwise, the sleeve is automatically centered by the spring-loaded balls, and the direction of v_6 does not matter if its absolute value is relative low. In the considered clutch, v_6 can be chosen within the range $|v_6| < 0.15$ m/s.

For a better understanding, the flowchart of sensorless disengagement is shown in Figure 9. The parameter values calculated using the method described above are shown in Table 1 for sensorless disengagement of the shift sleeve from both gearwheels to the neutral gear position. It can be seen that a higher disengaging speed, a lower braking current, and a later braking is chosen for the left side compared to the right side. This is done for the reason described below. When the sleeve teeth become disengaged, the driving motor is no longer loaded by the output shaft, which may lead to the fast increase of the countershaft rotation speed, and to the fast change of the relative speeds between the gearwheels and the output shaft as following. The left gear represents the overdrive gear, while the right gear is the underdrive gear. Consequently, compared to the disengagement of the right

gearwheel, the relative angular position and speed on the left side change faster when the left gearwheel becomes disengaged, so that the teeth may no longer be aligned with the slots even before $x = 0$ is reached. In this case, the braking force becomes much higher than the assumed value due to the decreased reluctance of the magnetic circuit (the axial distance between the teeth of the sleeve and the side surface of the complementary ring is 3 mm lower compared to the distance between the teeth and slot bottoms, Figure 1). To avoid a failed disengagement, the lower values of I_{brake} and $|x_4|$ and the higher value of v_2 are chosen for the left side.

Table 1. Motion parameters for sensorless disengagement to the neutral gear position.

Parameter	Symbol	Unit	Value (Left Side Disengagement)	Value (Right Side Disengagement)
Disengaging current	I_{diseng}	**A**	**19**	**19**
Braking current	I_{brake}	**A**	**16**	**19**
Initial current on the engaged side (holding current)	$I_{eng\,in}$	**A**	**2**	**2.5**
Average electromagnetic disengaging force	$F_{diseng\,av}$	N	200	200
Average electromagnetic braking force	$F_{brake\,av}$	N	100	120
Position and speed at the start of the disengagement	x_0	mm	−8	8
	v_0	m/s	0	0
Position and speed when the holding force becomes negligible	x_1	mm	−7.5	7.5
	v_1	m/s	0.2	−0.2
Position and speed when the de-excitation of the disengaging coil starts	x_2	mm	−5.5	6.9
	v_2	**m/s**	**0.6**	**−0.38**
Voltage induced on the engaged side which triggers the de-excitation of the disengaging coil	$U_{ind\,off}$	V	−0.42	−0.46
Position and speed when the de-excitation of the disengaging coil is finished	x_3	mm	−3.6	5.6
	v_3	m/s	0.73	−0.52
Position and speed when the excitation of the braking coil starts	x_4	**mm**	**−1.5**	**2**
	v_4	m/s	0.66	−0.52
Delay between the start of the disengaging coil de-excitation and start of the braking coil excitation	t_{delay}	ms	6	10
Position and speed when the excitation of the braking coil is finished	x_5	mm	0.3	0.4
	v_5	m/s	0.48	−0.3
Position and speed when the de-excitation of the braking coil starts	x_6	mm	2.2	−0.3
	v_6	**m/s**	**−0.1**	**0**
Delay between the starts of the excitation and de-excitation of the braking coil	t_{brake}	ms	13	8

Manually defined parameters are typed in bold. Further parameters are calculated using the actuator characteristics (Figures 4–6 and 8) and Equations (14)–(26).

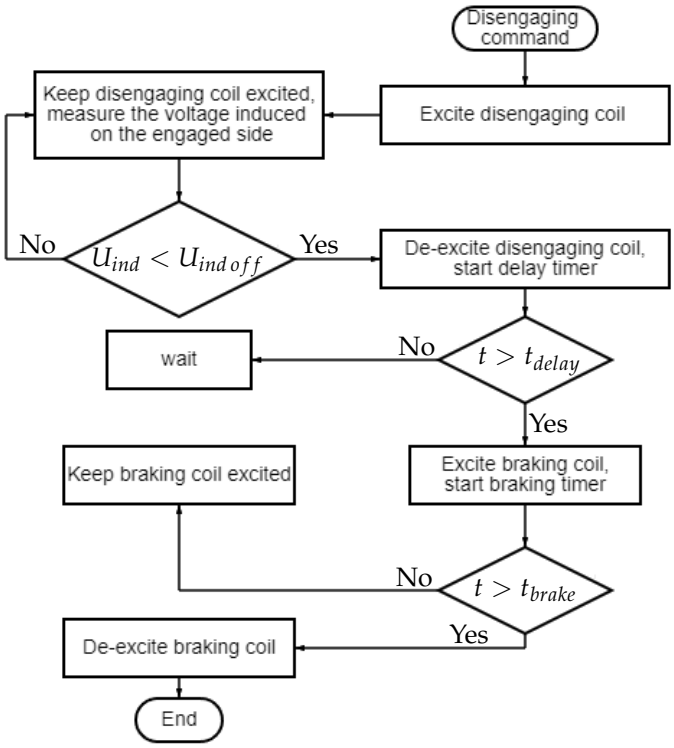

Figure 9. Flowchart of sensorless disengagement.

4. Simulation of Sensorless Disengagement

The proposed method of sensorless disengagement to the neutral gear position was tested under different conditions simulated in Matlab Simulink. All simulation results shown below were obtained using the following approach: the shift sleeve is initially completely engaged on one of the sides (the initial values of x are -7.95 mm if the left side is engaged and 7.95 mm if the right side is engaged, the deviation of 0.05 mm from the movement limits in Figure 1 is assumed due to the mentioned above reason, which is the impossibility to obtain a physical interval between the teeth and slots equal to zero in a real clutch); the output shaft with the sleeve rotate with a constant speed of the value n_{sleeve} during the entire simulation time; the initial θ_{rel} between the complementary ring and the shift sleeve is $-(\tau_s - \tau_t)/2 = -3^\circ$ (Figure 3c), so there is a mechanical contact between the side surfaces of the teeth and slots and the rotation of the output shaft is mechanically transmitted to the complementary ring as long as $|x| < 5$ mm, making the initial relative speed on the engaged side equal to zero and the initial speed of the countershaft n_c equal to $n_{sleeve}g_{eng}$, therefore, different initial relative speeds on the disengaged side of the value $n_c/g_{diseng} - n_{sleeve}$ can be obtained depending on the value of n_{sleeve}; the initial relative angle on the disengaged side is set manually; excepting F_{tilt}, which is very low, all electromagnetic and mechanical axial forces which act on the shift sleeve are considered in the simulation, and their sum results in the total axial force F_{sleeve}. To consider different torques that can act on the shift sleeve during the disengagement, the simulations have been conducted for different torques T_{motor} applied by the engine to the countershaft including $T_{motor} = 0$ (the engine is turned off / disconnected from the countershaft of the gearbox by releasing a clutch that couples the engine with the gearbox). To simplify the simulation, T_{shaft} is set to zero in all cases, making the initial resulting torque on the sleeve equal to $(T_{motor} - T_{cfr})g_{eng}$ (Equations (1) and (2)). Finally, the currents are controlled using proportional current control, the absolute value of the maximum voltage that can be applied to the coil based on the difference between the required and measured current is equal to the supply voltage $U = 70$ V.

Figure 10 shows the simulation results of the left gearwheel disengagement at the following conditions: n_{sleeve} = 3000 rpm, T_{motor} = −15 Nm, $T_{c\,fr}$ = 2.6 Nm, the initial relative angle on the disengaged right side $\theta_{rel\,right}$ = 10°. The results of the simulated switching between the left and neutral gears shown in Figure 11 were obtained under very different conditions: n_{sleeve} = 100 rpm, T_{motor} = 0 Nm, $T_{c\,fr}$ = 0.8 Nm, the initial $\theta_{rel\,right}$ = 4°. The initial left coil current is 2 A in both cases. A clear difference in the resulting force F_{sleeve} applied to the shift sleeve can be seen when comparing Figures 10 and 11. Also, the delayed braking, which is mentioned in the previous section, causes a relative high "overshoot" of the position $x = 0$. Nevertheless, the shift sleeve is successfully disengaged to the neutral gear position in both simulated cases without a mechanical impact on the opposite (right) side.

Figure 12 shows the results of the simulated right gearwheel disengagement at the initial values of n_{sleeve} = 800 rpm, T_{motor} = 0 Nm, $T_{c\,fr}$ = 2.2 Nm, and the initial relative angle on the disengaged left side $\theta_{rel\,left}$ = −16°. Finally, switching between the right and neutral gears at a low relative speed on the left side, which is delayed due to an unfavorable initial value of $\theta_{rel\,left}$, is shown in Figure 13, where the disengagement starts at the following conditions: n_{sleeve} = 50 rpm, T_{motor} = −10 Nm, $T_{c\,fr}$ = 0.75 Nm, $\theta_{rel\,left}$ = 14°. The initial current in the right coil is 2.5 A in both simulated situations. The results show that the "overshoot" of the neutral gear position $x = 0$ is much lower comparing to the disengagement of the left gearwheel since the braking is not delayed. The time elapsed between the start of the disengagement and the motion start in Figure 13 is about 60 ms, which are required to reach $\theta_{rel\,left} \approx 6°$ where $|F_{diseng}|$ becomes higher than $|F_{fr} + F_{hold}|$. Obviously, the delay can be reduced simply by making the initial current I_{right} lower. However, this may cause a higher error in the measurement of the induced voltage U_{ind} in real conditions. The reason is discussed in the next section.

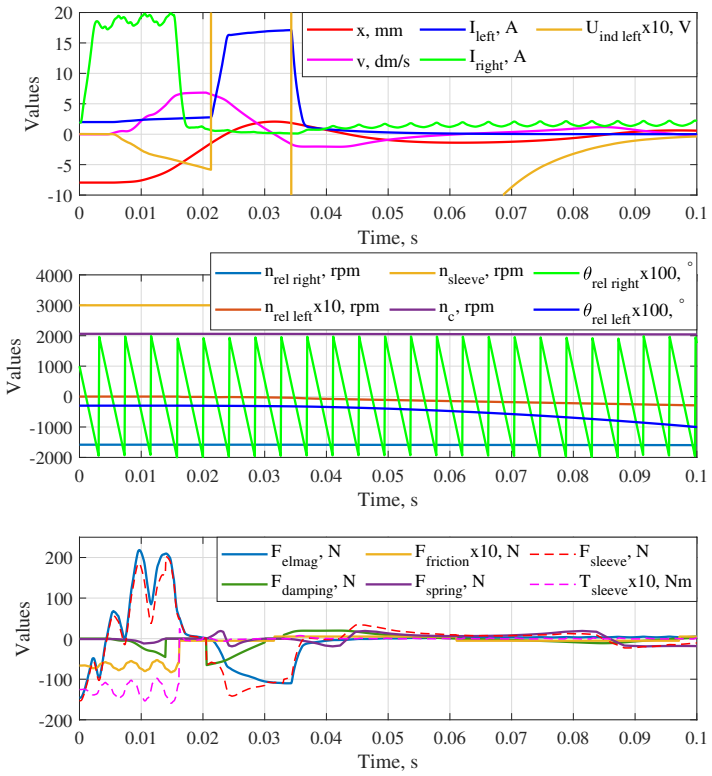

Figure 10. Simulation results of the sensorless shift sleeve disengagement from the left gearwheel to the neutral gear position at a high relative speed on the right side and higher friction force.

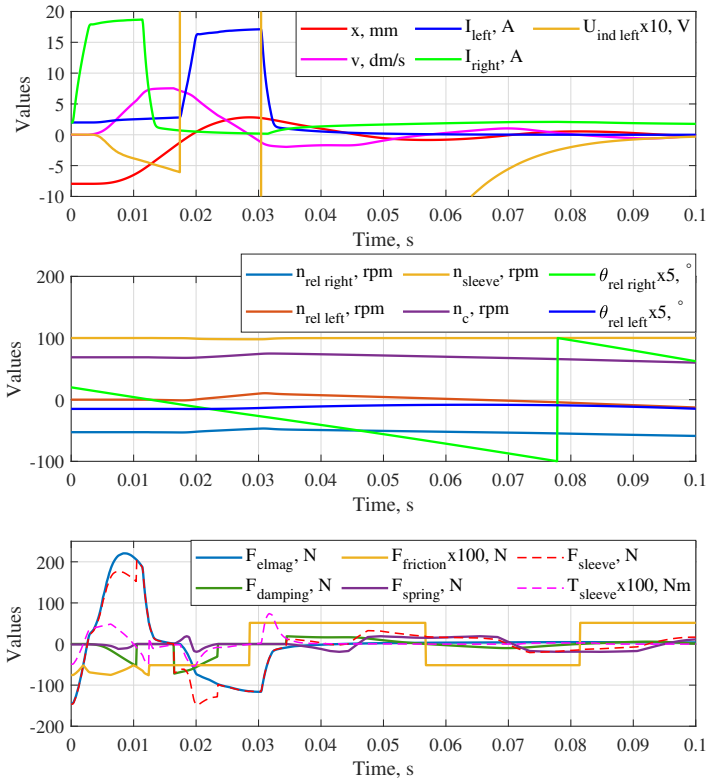

Figure 11. Simulation results of the sensorless shift sleeve disengagement from the left gearwheel to the neutral gear position at a low relative speed on the right side and lower friction force.

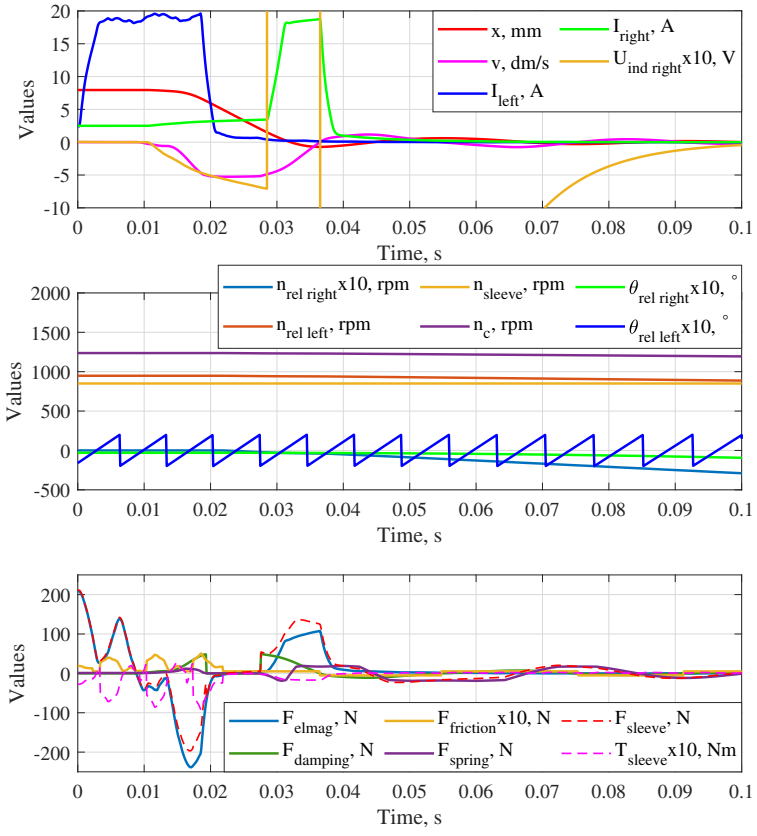

Figure 12. Simulation results of the sensorless shift sleeve disengagement from the right gearwheel to the neutral gear position at a medium relative speed on the left side and lower friction force.

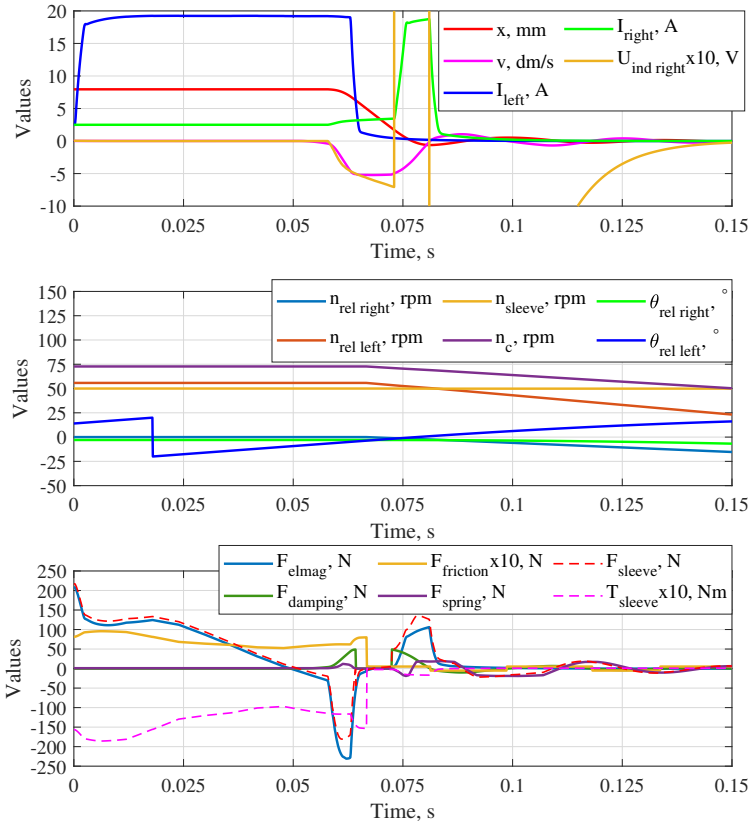

Figure 13. Simulation results of the sensorless shift sleeve disengagement from the right gearwheel to the neutral gear position at a low relative speed and unfavorable initial angle on the left side while the friction force is higher.

To evaluate the performance of the proposed method of sensorless disengagement, the stroke length of the actuator (the distance between two end-positions) and the settling time (time required for the mover to cover the distance between the end-positions and remain within a given error band of 10% after the application of the control impulse) is compared in Table 2 with those of other sensorless-controlled actuators presented in the scientific literature. It can be concluded that the developed method allows to shift the neutral gear with a relatively high speed. However, its main advantage it the applicability in linear-rotary actuators, where the inductance is represented by a function of three variables, namely the axial position, the (relative) angular position, and the coil current.

Table 2. Comparison of the actuator with sensorless-controlled actuators presented in the literature.

Actuator Type	Method of Sensorless Control	Stroke Length	Settling Time
Solenoid valve actuator [17]	Measurement of the incremental inductance	8 mm	∼0.5 s
Valve actuator with two coils [20]	Sliding mode observer	8 mm	0.01...0.02 s
Solenoid actuator [23]	Direct inductance measurement	6 mm	∼2 s
Compact dual solenoid actuator [26]	Injection of an additional AC signal	0.4 mm	∼1 s
Fast-switching solenoid actuator [22]	Sliding mode observer	0.42 mm	∼0.006 s
Linear reluctance actuator with two coils [27]	Measurement of the back electromotive force	10 mm	0.05...0.07 s
Solenoid electromagnet [28]	Estimation of the change in the coil impedance	15 mm	∼4 s
Linear-rotary reluctance actuator with two coils (this work)	*Measurement of the induced voltage and motion prediction*	*8 mm*	*0.03...0.07 s*

5. Experimental Results

The proposed method of sensorless gear switching has been verified on the testrig shown in Figure 14, which includes two motors, the torque sensor, and the actuator prototype installed inside the testing gearbox. Motor 1 is coupled with the output shaft, on which the shift sleeve is placed, and motor 2 with the countershaft of the gearbox via the torque sensor. The countershaft is connected with the left and right complementary rings via intermediate shafts and two belt transmissions with the gear ratios 44/64 and 64/44 on the left and right side, respectively. The structure and components of the testrig are described in detail in [14].

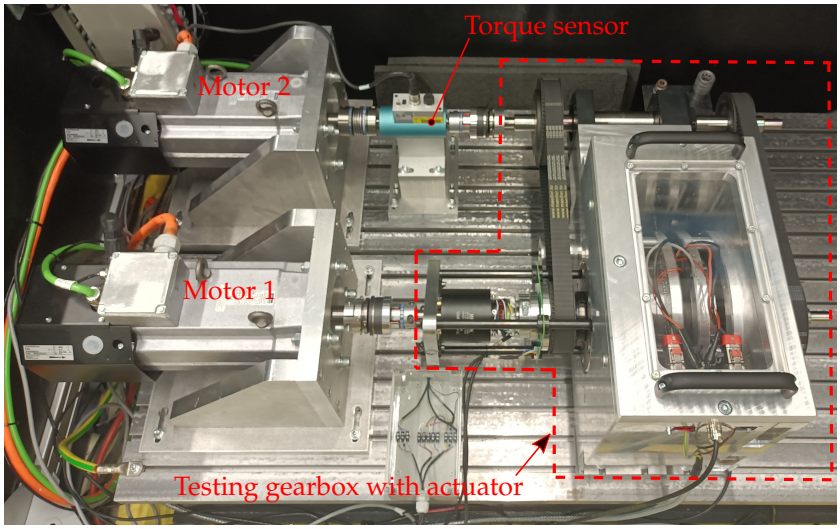

Figure 14. Testrig with the actuator prototype installed inside the testing gearbox.

The experimental results that are shown in Figures 15, 16, 17, and 18 were obtained creating conditions on the testrig which are similar to the simulated conditions of Figures 10, 11, 12, and 13, respectively. The main differences between the experiments and the simulations are listed below. Firstly, there is considerable noise in the current signals, the noise intensity is in the range between −0.15 and 0.15 A, therefore, the induced voltage was filtered using a low-pass filter, which delays the signal change. To take into account this fact, the values of $U_{ind\,off}$ from Table 1, which trigger the de-excitation of the disengaging

coil, were reduced by 10%. Secondly, the coil resistances increase linearly with the rising coil temperatures, so the resistance change was considered by measuring the coil temperatures with the thermistors placed on the coils and connected to the electronic control unit (ECU). Thirdly, it is not feasible to apply a significant torque T_{motor} to the countershaft by motor 2 and simultaneously keep the initial rotation speeds without applying a torque of the opposite direction to the output shaft by motor 1. Thus, in the experiments with the loaded shift sleeve (Figures 15 and 18), motor 2 generated positive torques of the values T_{motor} = 15 Nm and 10 Nm, respectively, while motor 1 was controlled to keep the initial speed of the output shaft, generating a negative torque T_{shaft}. The rotation speeds does not change if $T_{shaft} \approx -(T_{motor} - T_{c\,fr})g_{eng}$. The resulting initial value of T_{sleeve} can be estimated in this case as $T_{sleeve} \approx 2(T_{motor} - T_{c\,fr})g_{eng}$. If the friction torque $T_{c\,fr}$ has the same values as in the simulations (2.6 and 0.75 Nm for Figures 15 and 18, respectively), $T_{sleeve} \approx 24.8$ Nm in the experiment with the disengagement of the left gearwheel under load (Figure 15) and $T_{sleeve} \approx 18.5$ Nm in the experiment which results are shown in Figure 18. In these two cases, the torque on the countershaft, which was measured with the torque sensor, is indicated in the corresponding figures as T_c.

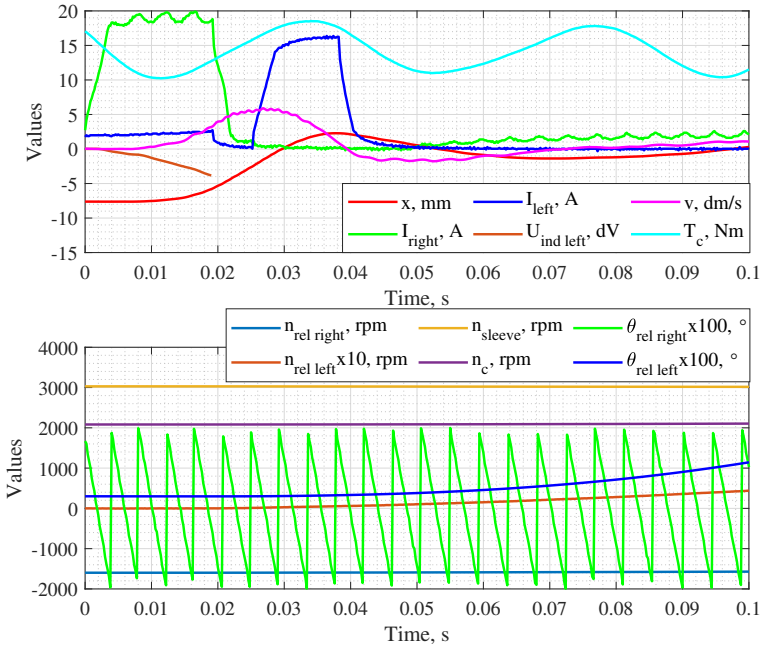

Figure 15. Experimental results of the sensorless shift sleeve disengagement from the left gearwheel to the neutral gear position at a high relative speed on the right side and higher friction force.

The experimental results confirm the suitability of the proposed method for sensorless disengagement to the neutral gear position. In all four cases, the shift sleeve was disengaged to the neutral gear position without an impact on the opposite side or stopping before x = 0 was reached. In Figure 17, the initial value of the voltage U_{ind} induced on the engaged right side is false (non-zero). This is explained by that fact that the voltage applied by the ECU to the coil deviates from the required voltage if the temperature of the ECU changes, and this deviation is especially high at very low duty cycles. Since the voltage of the power supply was set equal to the maximum available value of 70 V to achieve the fastest possible current dynamic, the initial current of 2.5 A on the engaged right side corresponds to the DC-voltage of 1.875 V or 2.7% duty cycle. This is the reason why a lower initial current was not chosen to expand the starting range of $\theta_{rel\,diseng}$. Despite the error in the measurement of U_{ind}, the neutral gear was successfully shifted.

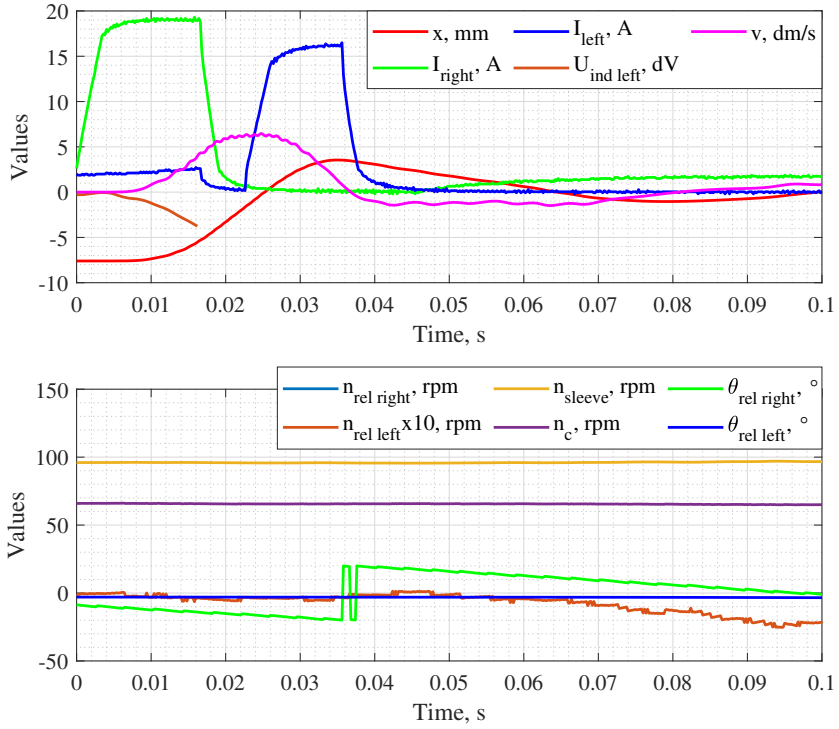

Figure 16. Experimental results of the sensorless shift sleeve disengagement from the left gearwheel to the neutral gear position at a low relative speed on the right side and lower friction force.

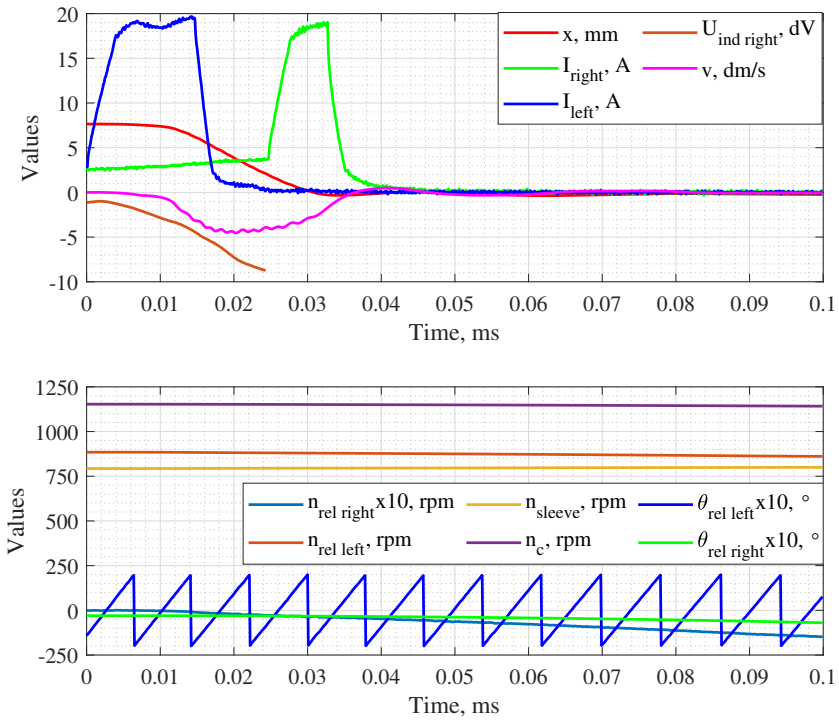

Figure 17. Experimental results of the sensorless shift sleeve disengagement from the right gearwheel to the neutral gear position at a medium relative speed on the left side and lower friction force.

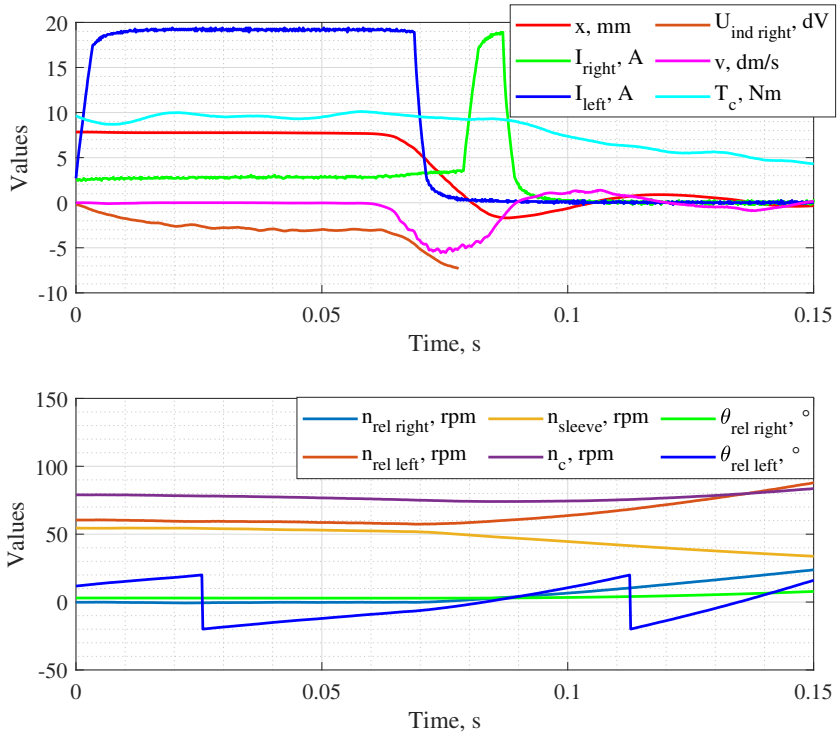

Figure 18. Experimental results of the sensorless shift sleeve disengagement from the right gearwheel to the neutral gear position at a low relative speed and unfavorable initial angle on the left side while the friction force is higher.

To evaluate the deviance between the simulation results and the experimental results, the settling time t_s and the maximum travel distance d were measured. The settling time corresponds to the time elapsed between the start of the disengagement and the stabilization of the shift sleeve movement within the band ± 1 mm, and the maximum travel distance is the the maximum distance the shift sleeve moves from the starting point x_0 during the disengagement. t_s and d are given for each disengagement condition in Table 3, where the values obtained in the simulations have the index sim, and the experimentally obtained values have the index exp. Then, the settling time error e_s and the travel distance error e_d were calculated for each case as

$$e_s = \frac{t_{s\,exp} - t_{s\,sim}}{t_{s\,sim}}, \tag{27}$$

$$e_d = \frac{d_{exp} - d_{sim}}{d_{sim}}. \tag{28}$$

The values of e_s and e_d are also given in Table 3 for all considered cases. The settling time error is very low in the cases when no torque is applied to the countershaft ($T_{motor} = 0$) but increases when T_{motor} is nonzero. This is explained by the experimental limitations mentioned above (T_{shaft} must be nonzero if $T_{motor} \neq 0$), which result in a much higher torque transmitted through the shift sleeve. However, the travel distance error, which is much more important for a safe shifting into neutral, is low in all considered cases.

Additional experiments, which were conducted under different conditions, can be seen in the Supplementary Videos S1–S6.

Table 3. Values of the settling times and maximum travel distances obtained in the simulations and experiments and their errors.

Disengagement Condition	$t_{s\,sim}$	$t_{s\,exp}$	e_s	d_{sim}	d_{exp}	e_d
Disengagement of the left gearwheel (n_{sleeve} = 3000 rpm and T_{motor} = −15 Nm)	0.071 s	0.082 s	20 %	10 mm	10.3 mm	3 %
Disengagement of the left gearwheel (n_{sleeve} = 100 rpm and T_{motor} = 0)	0.056	0.058 s	4 %	10.8 mm	11.5 mm	6 %
Disengagement of the right gearwheel (n_{sleeve} = 800 rpm and T_{motor} = 0)	0.029 s	0.027 s	−7 %	8.7 mm	9.7 mm	11 %
Disengagement of the right gearwheel (n_{sleeve} = 50 rpm and T_{motor} = −10 Nm)	0.074 s	0.096 s	30 %	8.6 mm	8.3 mm	−3 %

6. Conclusions

The method of shift sleeve disengagement to the neutral gear position without a linear encoder placed inside the gearbox is developed in this paper. The algorithm is based on the electromechanical model of the double-sided electromagnetic dog clutch. Some average values of the accelerating and braking forces can be assumed, which allows to predict the motion of the shift sleeve. Eddy currents, which arise in the massive steel of the clutch parts, are considered based on their simplified model developed earlier. It is shown that different pre-defined parameters (such as the holding and braking currents, the position to start the braking, and the residual motion speed) can be selected for the clutch sides considering different gear ratios.

At its current state of development, the method requires thermistors placed on the coils to measure their temperatures, but they are much cheaper and reliable than a magnetic encoder exposed to the aggressive environment inside the gearbox. The algorithm can be implemented very simply and does not require an injection of any additional signals. However, its main advantage is that angular encoders are also not required despite the coil inductances are highly dependent on the relative angle between the teeth and slots.

The algorithm was tested under different conditions in the simulations and verified experimentally. The suitability for different (relative) rotation speeds, that can be presented in the gearbox, and different resulting torques on the shift sleeve is shown. Moreover, the developed sensorless control works stable despite disturbances such as an error in the measured induced voltage.

It the future, the proposed algorithm can be extended with a method for thermal compensation, so the measurement of the coil temperatures will be no longer required.

7. Patents

Miroschnitschenko, B.; Poltschak, F.; Rafetseder, D. Electromechanical clutch and method for closing and opening an electromechanical clutch and for sensorless determination of the relative angular velocity of a first and second shaft. DE102022121714A1, February 2024.

Supplementary Materials: The following supporting information can be downloaded at: https://www.mdpi.com/article/10.3390/act14100484/s1, Video S1: Sensorless disengagement of left gearwheel (200 rpm), Video S2: Sensorless disengagement of left gearwheel (1000 rpm), Video S3: Sensorless disengagement of left gearwheel (3000 rpm), Video S4: Sensorless disengagement of right gearwheel (500 rpm), Video S5: Sensorless disengagement of right gearwheel (1000 rpm), Video S6: Sensorless disengagement of right gearwheel (1500 rpm).

Funding: This work was conducted as a fundamental research project at the Hoerbiger Research Institute for Smart Actuators, which is funded by Hoerbiger Foundation, Zug, Switzerland.

Data Availability Statement: The data presented in this study are available upon request from the author.

Acknowledgments: The publication of this research was supported by Johannes Kepler Open Access Publishing Fund and the federal state Upper Austria.

Conflicts of Interest: The author declares no conflicts of interest. The funders had no role in the design of the study; in the collection, analysis, or interpretation of data; in the writing of the manuscript.

Abbreviations

The following abbreviations are used in this manuscript:

SRM	Switched reluctance machine
LRRA	Linear-rotary reluctance actuator
SE	Solenoid electromagnet
DoF	Degree of freedom
FEA	Finite element analysis
ECU	Electronic control unit

References

1. Poltschak, F.; Rafetseder, D.; Miroschnitschenko, B. Electromagnetic direct drives for positive mechanical engagement in the automotive drivetrain. In Proceedings of the Tagungshandbuch Symposium Elektromagnetismus, Künzelsau, Germany, 27–28 February 2025; pp. 93–100.
2. Poltschak, F.; Rafetseder, D. Completely integrated electromagnetic dog clutch actuator for automotive applications. In Proceedings of the IKMT 2022; 13. GMM/ETG-Symposium, Linz, Austria, 14–15 September 2022; pp. 1–6.
3. Jeong, W.; Han, J.; Kim, T.; Lee, J.; Oh, S. Two-speed transmission structure and optimization design for electric vehicles. *Machines* **2023**, *12*, 9.
4. Pan, T.; Zang, H.; Wu, P. Hierarchical mode optimization strategy for gear engagement process of automated manual transmission with electromagnetic actuator. *Proc. Inst. Mech. Eng. Part D J. Automob. Eng.* **2023**, *237*, 913–929.
5. Stetter, R.; Göser, R.; Gresser, S.; Witczak, M.; Till, M. Fault-Tolerant Design of a Gear Shifting System for Autonomous Driving. In Proceedings of the Design Society: DESIGN Conference, Online, 26–29 October 2020; Cambridge University Press: Cambridge, UK, 2020; Volume 1, pp. 1125–1134.
6. Aljawabrah, A. Analysis and Control of the Gearshift Process Based on a Dog Clutch Shiftability Model. *Cogn. Sustain.* **2024**, *3*. https://doi.org/10.55343/CogSust.120.
7. Lu, Z.; Tian, G. Time-optimal coordination gear-shifting control with a rotational angle difference estimation and alignment algorithm in the vehicle-start condition. *IEEE Trans. Transp. Electrif.* **2024**, *10*, 9000–9015.
8. Gongye, X.; Du, C.; Huang, C.; Huang, J.; Wang, J. Research on gearshift of Non-synchronizer automatic mechanical transmission based on hierarchical bounding box collision detection algorithm. *Energy Rep.* **2025**, *13*, 1200–1214.
9. Miroschnitschenko, B. Magnetic flux calculation in a novel linear-rotary electromagnetic actuator using 3d magnetic equivalent circuit. In Proceedings of the 2023 11th International Conference on Control, Mechatronics and Automation (ICCMA), Agder, Norway, 1–3 November 2023; pp. 336–345.
10. Tsai, M.C.; Huang, C.C.; Huang, Z.Y. A new two-phase homopolar switched reluctance motor for electric vehicle applications. *J. Magn. Magn. Mater.* **2003**, *267*, 173–181.
11. Miroschnitschenko, B.; Amrhein, W.; Poltschak, F. Design and Optimization of a Linear-Rotary Electromagnetic Actuator Based on Analytical Model of Magnetic Flux. In Proceedings of the 2024 International Symposium on Power Electronics, Electrical Drives, Automation and Motion (SPEEDAM), Ischia, Italy, 19–21 June 2024; pp. 1002–1009.
12. Wanli, X.; Wei, Z.; Bin, S.; Ximeng, X. Investigation of manual transmission synchronizer failure mechanism induced by interface material/lubricant combinations. *Wear* **2015**, *328*, 475–479.
13. Barathiraja, K.; Devaradjane, G.; Paul, J.; Rakesh, S.; Jamadade, G. Analysis of automotive transmission gearbox synchronizer wear due to torsional vibration and the parameters influencing wear reduction. *Eng. Fail. Anal.* **2019**, *105*, 427–443.
14. Miroschnitschenko, B.; Poltschak, F.; Amrhein, W. A novel double-sided electromagnetic dog clutch with an integrated synchronizer function. *Actuators* **2025**, *14*, 286.

15. Miroschnitschenko, B.; Polschak, F.; Rafetseder, D. Electromechanical clutch and method for closing and opening an electromechanical clutch and for sensorless determination of the relative angular velocity of a first and second shaft. Patent Application DE102022121714A1, 29 February 2024. Available online: https://patents.google.com/patent/DE102022121714A1/en?oq=de102022121714a1 (accessed on 3 October 2025).
16. Miroschnitschenko, B.; Poltschak, F.; Amrhein, W. Sensorless Estimation of Relative Angular Position and Speed in a Linear-Rotary Reluctance Actuator with High Influence of Eddy Currents. In Proceedings of the 2025 19th Conference on Electrical Machines, Drives and Power Systems (ELMA), Sofia, Bulgaria, 19–21 June 2025; pp. 1–6.
17. Rahman, M.F.; Cheung, N.C.; Lim, K.W. Position estimation in solenoid actuators. *IEEE Trans. Ind. Appl.* **1996**, *32*, 552–559.
18. Dülk, I.; Kovácsházy, T. Sensorless position estimation in solenoid actuators with load compensation. In Proceedings of the 2012 IEEE International Instrumentation and Measurement Technology Conference Proceedings, Graz, Austria, 13–16 May 2012; pp. 268–273.
19. Maridor, J.; Katic, N.; Perriard, Y.; Ladas, D. Sensorless position detection of a linear actuator using the resonance frequency. In Proceedings of the 2009 International Conference on Electrical Machines and Systems, Tokyo, Japan, 15–8 November 2009; pp. 1–6.
20. Eyabi, P.; Washington, G. Modeling and sensorless control of an electromagnetic valve actuator. *Mechatronics* **2006**, *16*, 159–175.
21. Sarmad Qureshi, M.; Bebek, O. Sensorless position control of solenoid actuators for soft landing using super-twisting sliding mode control. *Proc. Inst. Mech. Eng. Part D J. Automob. Eng.* **2023**, *237*, 2565–2579.
22. Braun, T.; Reuter, J.; Rudolph, J. Observer design for self-sensing of solenoid actuators with application to soft landing. *IEEE Trans. Control Syst. Technol.* **2018**, *27*, 1720–1727.
23. König, N.; Grasso, E.; Nienhaus, M. Sensorless Closed-Loop Control of Solenoid Actuators Using IDIM Technique. In Proceedings of the 2018 AEIT International Annual Conference, Bari, Italy, 3–5 October 2018; pp. 1–6.
24. König, N.; Nienhaus, M. A solution to ambiguities in position estimation for solenoid actuators by exploiting eddy current variations. *Sensors* **2020**, *20*, 3441.
25. Nagai, S.; Kawamura, A. Sensorless position estimation with thermal compensation for compact dual solenoid actuator. In Proceedings of the IECON 2018-44th Annual Conference of the IEEE Industrial Electronics Society, Washington, DC, USA, 21–23 October 2018; pp. 2781–2786.
26. Nagai, S.; Kawamura, A. Sensorless position control for compact dual solenoid actuator using disturbance observer. In Proceedings of the 2019 IEEE International Conference on Mechatronics (ICM), Ilmenau, Germany, 18–20 March 2019; Volume 1, pp. 97–101.
27. Park, J.M.; Jung, J.W.; Kim, E.K.; Yoon, H.M.; Sung, J.M.; Yoon, J.Y. Energy-Efficient PM-Flux-Based Sensorless Soft Landing Control for Binary Electromagnetic Actuator. *IEEE/ASME Trans. Mechatronics* **2024**, *30*, 2790–2798.
28. Pawelczak, D.; Trankler, H.R. Sensorless position control of electromagnetic linear actuator. In Proceedings of the 21st IEEE Instrumentation and Measurement Technology Conference (IEEE Cat. No. 04CH37510), Como, Italy, 18–20 May 2004; Volume 1, pp. 372–376.
29. Akita, J. Solenoid Stroke Measurement Method Using Two Points of PWM Drive Current. *IEEJ Trans. Electr. Electron. Eng.* **2025**, *20*, 1608–1613.
30. Kramer, T.; Weber, J. Self-sensing position determination on a sensor-designed proportional solenoid. In Proceedings of the 12th International Fluid Power Conference (12. IFK), Dresden, Germany, 12–14 October 2020.
31. Reinholz, B. Sensorless Plunger Position Control and Differential Plunger Position Self-Sensing Using Constant Air Gap Solenoids. Ph.D. Thesis, University of British Columbia, Vancouver, BC, Canada, 2022.
32. Rafetseder, D.; Poltschak, F. Position-Sensorless Control and End-Position Monitoring of a Two-Point Switching Actuator. In Proceedings of the 2024 International Symposium on Power Electronics, Electrical Drives, Automation and Motion (SPEEDAM), Ischia, Italy, 19–21 June 2024; pp. 209–214.
33. Martins, R.; Seabra, J.; Brito, A.; Seyfert, C.; Luther, R.; Igartua, A. Friction coefficient in FZG gears lubricated with industrial gear oils: Biodegradable ester vs. mineral oil. *Tribol. Int.* **2006**, *39*, 512–521.

Disclaimer/Publisher's Note: The statements, opinions and data contained in all publications are solely those of the individual author(s) and contributor(s) and not of MDPI and/or the editor(s). MDPI and/or the editor(s) disclaim responsibility for any injury to people or property resulting from any ideas, methods, instructions or products referred to in the content.